Buffered high charge spectrally-peaked proton beams in the relativistic-transparency regime

2016 New J. Phys. 18 013038

(http://iopscience.iop.org/1367-2630/18/1/013038)

New Journal of Physics
The open access journal at the forefront of physics

Deutsche Physikalische Gesellschaft DPG
IOP Institute of Physics

Published in partnership with: Deutsche Physikalische Gesellschaft and the Institute of Physics

OPEN ACCESS

RECEIVED
11 June 2015

REVISED
3 December 2015

ACCEPTED FOR PUBLICATION
15 December 2015

PUBLISHED
18 January 2016

PAPER

Buffered high charge spectrally-peaked proton beams in the relativistic-transparency regime

N P Dover[1], C A J Palmer[1], M J V Streeter[1], H Ahmed[2], B Albertazzi[3], M Borghesi[2], D C Carroll[4,5], J Fuchs[3], R Heathcote[5], P Hilz[6,7], K F Kakolee[2,8], S Kar[2], R Kodama[9], A Kon[9], D A MacLellan[4], P McKenna[4], S R Nagel[1], D Neely[4,5], M M Notley[5], M Nakatsutsumi[3,10], R Prasad[2,11], G Scott[4,5], M Tampo[9], M Zepf[2], J Schreiber[6,7] and Z Najmudin[1]

[1] The John Adams Institute for Accelerator Science, Blackett Laboratory, Imperial College, London SW7 2BZ, UK
[2] Centre for Plasma Physics, Queen's University Belfast BT7 1NN, UK
[3] LULI, École Polytechnique, CNRS, CEA, Palaiseau, France
[4] SUPA Department of Physics, University of Strathclyde, Glasgow G4 0NG, UK
[5] Central Laser Facility, STFC Rutherford Appleton Laboratory, Oxfordshire OX11 0QX, UK
[6] Fakultät für Physik, Ludwig-Maximilians-Universität München, Am Coulombwall 1, D-85748 Garching, Germany
[7] Max-Planck-Institut für Quantenoptik, Hans-Kopfermann-Str. 1, D-85748 Garching, Germany
[8] Jagannath University, Dhaka, Bangladesh
[9] Graduate School of Engineering, Osaka University, Osaka D-565-0871, Japan
[10] European XFEL, GmbH, Albert-Einstein-Ring 19, 22671 Hamburg, Germany
[11] Institute for Laser and Plasma Physics, Heinrich Heine University, Düsseldorf, D-40225, Germany

E-mail: nicholas.dover08@imperial.ac.uk

Keywords: laser–plasma interaction, ion acceleration, laser ion source, proton acceleration

Supplementary material for this article is available online

Abstract

Spectrally-peaked proton beams of high charge ($E_p \approx 8$ MeV, $\Delta E \approx 4$ MeV, $N \approx 50$ nC) have been observed from the interaction of an intense laser ($>10^{19}$ W cm^{-2}) with ultrathin CH foils, as measured by spectrally-resolved full beam profiles. These beams are reproducibly generated for foil thicknesses 5–100 nm, and exhibit narrowing divergence with decreasing target thickness down to ≈8° for 5 nm. Simulations demonstrate that the narrow energy spread feature is a result of buffered acceleration of protons. The radiation pressure at the front of the target results in asymmetric sheath fields which permeate throughout the target, causing preferential forward acceleration. Due to their higher charge-to-mass ratio, the protons outrun a carbon plasma driven in the relativistic transparency regime.

1. Introduction

The interaction of high intensity lasers with opaque plasma has been widely investigated as a source of multi-MeV ions. Irradiation of micron thick foils at high laser intensity produces sheath fields that can accelerate protons [1, 2]. However, these beams characteristically have a thermal spectrum. Limiting the energy spread of these beams, especially reducing low energy parasitic ions, is a key objective in this field. Schemes to reduce the energy spread of sheath accelerated beams often rely on spatially localising the protons within a mixed species foil. This was demonstrated by manufacturing targets with the required ion species localised on the target rear surface [3–5]. A similar effect can be achieved by pre-expanding the foil [6], so that protons can be separated from a trailing lower charge-to-mass ratio host ion species.

Simulations have shown species separation also occurs when a single high-intensity pulse interacts with multi-species thin ($\lesssim$100 nm) targets [7–9]. For target thickness comparable to the skin-depth, $d_0 \lesssim \sqrt{\gamma}\,(c/\omega_p)$, species separation rapidly occurs due to laser field penetration into the target [8, 9]. The target remains opaque during the interaction if $d_0 \gtrsim d_{rt} \equiv (\gamma n_c/n_{e0})c_s\tau_L$, where γn_c is the relativistic critical density, n_{e0} is the initial electron density, the expansion time is the laser pulse duration τ_L, and c_s is the target surface sound speed; expansion towards the laser is suppressed by radiation pressure. The foil can then be accelerated by light sail radiation pressure acceleration (RPA) [12–17]. Spectrally peaked proton beams from 10 to 100 nm foils

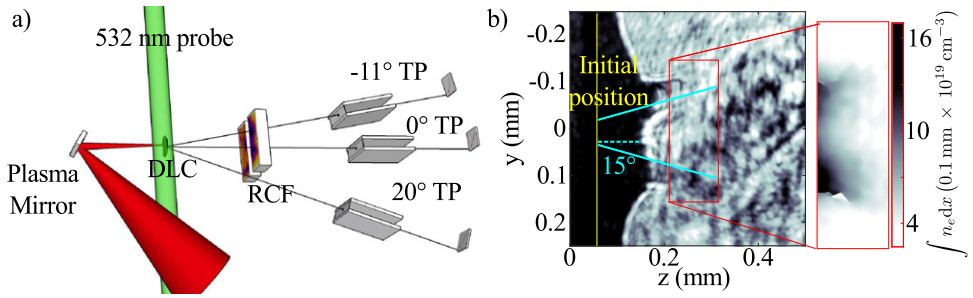

Figure 1. (a) Experimental set-up. (b) Probe shadowgraphy at $t = 250$ ps after the interaction together with phase map, in units of the line density integral, from simultaneous interferometry (red box) for $d_0 = 100$ nm, LP. The yellow line indicates the initial position of the rear surface measured before the shot.

accelerated in the light sail regime have been reported using high-Z foils with $\tau_L \sim 1$ ps [10] or carbon foils with $\tau_L \sim 50$ fs [11]. The proton layer is spatially separated from, and accelerated ahead of, the higher-Z species. RPA can be disrupted by the transverse instabilities that form at the laser–plasma interface [18], but due to the spatial separation from this unstable region the protons can be insulated from these instabilities, and can be considered to be 'buffered' by the higher-Z species [9]. Although the plasma fields are strongly transversely modulated in the unstable region, the large angular divergence of locally accelerated electrons results in smoother accelerating space charge fields away from this region.

If the target becomes relativistically transparent during the laser–plasma interaction ($d_0 \lesssim d_{rt}$), RPA is suppressed, and an increase in the coupling of the laser energy to thermal electrons drives a rapid asymmetric expansion of the plasma [21]. Recent experiments have demonstrated enhanced acceleration from targets driven in this regime [19–23]. Removing protons prior to interaction with relativistically transparent targets resulted in higher carbon energies [24]. Simulations of multi-species targets in this regime also exhibit buffering of protons [7].

We present the first experimental measurements of fully spatially characterised spectrally-peaked proton beams from any laser-solid target ion acceleration experiment. We use relatively long laser duration ($\tau_L \sim 1$ ps) combined with nanometre-thickness carbon foils to *thermally drive* the acceleration, in contrast to previous experiments showing spectrally modulated beams from RPA [10, 11]. The narrow energy spread proton beams were observed for the first time from a thermally driven foil without the need for target microstructures or deliberate pre-expansion. The high charge (≈50 nC) beams had typical peak energy $E_p \approx 8$MeV, corresponding to the velocity of the carbon ion front, and $\Delta E \approx 4$ MeV. Spatial profile measurements also revealed a novel plasma lensing effect in which the beam divergence reduced with decreasing target thickness d_0 to ≈8° for 5 nm foils. Numerical simulations, consistent with the experiment, demonstrate that the target becomes relativistically transparent to the laser. The majority of the ion energy gain occurs in this phase, not from RPA. The protons are spatially separated from and buffered ahead of the heavier carbon ions while being protected from transverse instabilities dominating the carbon species. This generation of highly collimated, high charge, narrow energy spread beams devoid of a low-energy parasitic component is ideal for numerous applications, such as radioisotope generation or injection into accelerators.

2. Experimental results

The experiment was performed using Vulcan Petawatt ($\lambda = 1.054$ μm) at the Rutherford Appleton Laboratory. The experimental set-up is shown in figure 1(a). A plasma mirror irradiated at 3×10^{14} W cm^{-2} enhanced the laser contrast to ≈10^{-10} [25]. The resulting (130 ± 20) J, τ_L≈ 700 fs pulse was $f/3$ focussed with 35% of the energy within a focal spot ($1/e^2$) width $w_0 = 8$ μm, measured at low power. The implied full power intensity is therefore $I_L \approx 1 \times 10^{20}$ W cm^{-2}, assuming no difference at focus between low and high power. The laser was either linearly polarised (LP) in the vertical direction or, by inserting a zero-order $\lambda/4$ waveplate (92 % energy transmission) in the focussing beam before the plasma mirror, circularly (CP) polarised. The transmission of s- and p- polarisation through the plasma mirror was measured to be 68% and 72% respectively, and the $\lambda/4$ waveplate optical axis was rotated to account for this. The laser was normally incident onto diamond-like carbon (DLC) foils of thickness $d_0 \in$ 5–500 nm, which were rear mounted on a circular aperture of 1 mm diameter. The foils had a density $\rho \approx 2.8$ g cm^{-3} and comprised of an estimated ≈90% C/10% H in the bulk (from elastic recoil detection analysis) [26]. They also form an additional nanometre-scale hydrocarbon impurity layer before laser irradiation.

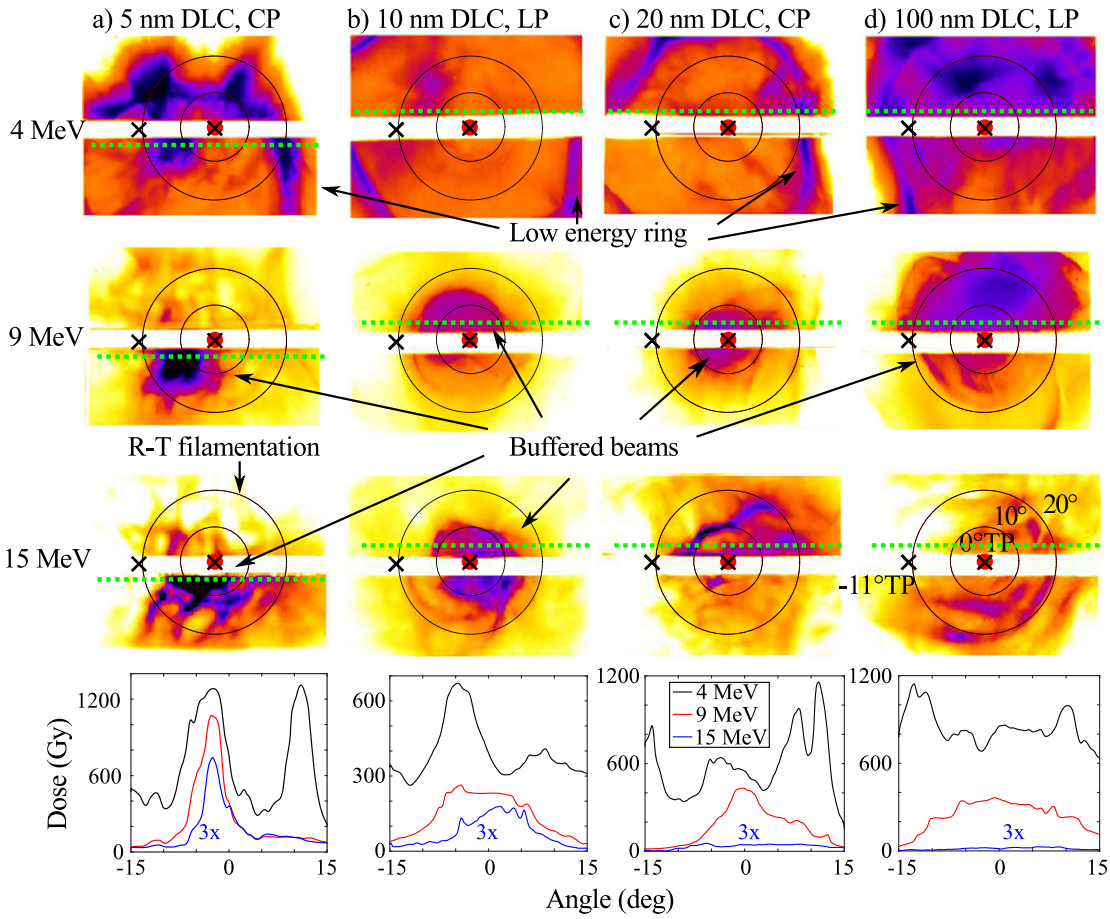

Figure 2. (a)–(d) Proton beam profiles from $d_0 = 5, 10, 20, 100$ nm using CP, LP, CP, LP respectively at 4, 9, 15 MeV. Red dot represents laser-axis, and black rings are at 10, 20° full-cone angle. The 0, −11° TP are indicated with black crosses. (20° TP is off the right edge). All films are contrast enhanced, and dark colour represents higher dose. Dose line outs from the dotted green lines for each target thickness are given in the bottom row. The $E = 15$ MeV line out has been multiplied by 3.

The proton beam profile was diagnosed using a radiochromic film (RCF) stack, allowing observation within $\lesssim$30° full-angle. The dose deposited in each layer of the stack is dominated by a small range of proton energies, E, which have their Bragg peak in the sensitive layer in the RCF. There is a further lesser contribution from higher energy particles which deposit a small fraction of their energy as they slow down in the layer [27]. Carbon ions would require >80 MeV to reach the RCF. Only small numbers of C ions were measured at these high energies and carbon was therefore assumed to contribute negligible dose to the RCF stack. High-resolution spectra were recorded using three Thomson parabola (TP) spectrometers. The TP sampled 0°, −11°and +20° behind a horizontal gap in the stack (figure 2). TP use co-linear magnetic and electric fields to separate and disperse ions by charge-to-mass ratio and energy, with the resultant signal measured using imaging plate detectors [29]. The combination of these diagnostics allows combined spatial and high resolution spectral measurement of the proton beam.

Additionally an optical probe beam ($\lambda = 532$ nm) passed transversely across the target rear surface with an adjustable time delay with respect to the intense pulse before being split into shadowgraphy and Mach–Zender interferometry. An example shadowgraphy image taken 250 ps after the irradiation of a 100 nm target with LP is shown in figure 1(b). A clear cone like structure is seen on the shadowgraphy, and processed interferometry shows a significant reduction of the electron density along the laser-axis. Such a plasma distribution was typical of all the foils in this thickness range. We note that this differs from previous optical probing performed on thin foils driven by radiation pressure on Vulcan Petawatt, which show typically isotropic expansion from the focal region [28].

Examples of proton beam profiles are shown for CP and LP with $d_0 = 5$–100 nm in figures 2(a)–(d) (full datasets are available in the supplemental data). For $E = 4$ MeV, the beam is dominated by an annular ring with divergence angle >20°. This ring structure was characteristic for all polarisations and thicknesses. On occasion the ring structure was directed into the −11° TP revealing a high-flux ($\approx 5 \times 10^{12}$ MeV^{-1} sr^{-1}) broadband beam

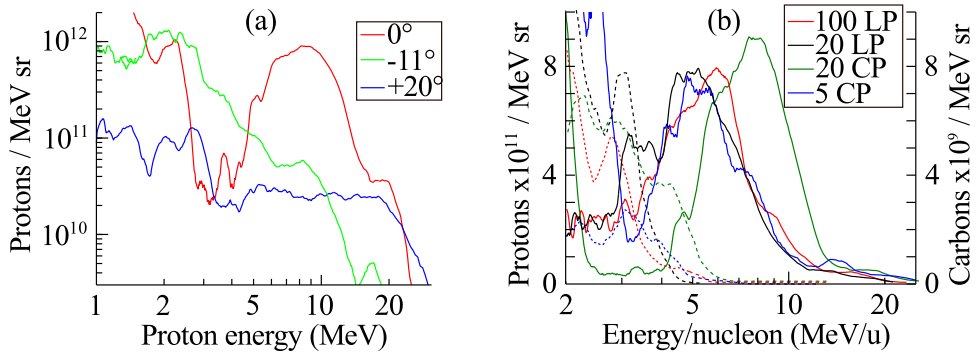

Figure 3. (a) H^+ spectra from all TPs from CP, 20 nm target (figure 2(c)) on a logarithmic scale. (b) H^+ (solid) and C^{6+} ion (dashed) spectra on 0° TP for different polarisations/thickness (in nm) with a linear ion number scale. The 5 nm (CP) corresponds to shot in figure 2(a) and the 20 nm (CP) corresponds to figure 2(c).

with energy up to $E_{max} \approx 5$ MeV. The emission angle of the annular ring is similar to the plasma expansion of the cone seen on the optical probe (figure 1(b)).

For $E = 9$ MeV, the annular ring has disappeared for all target thicknesses. Instead, a more collimated circular beam is seen near the laser-axis for $d_0 \leqq 100$ nm, which is not always present for $E = 4$ MeV. This beam has a full-angle divergence $<20°$, and becomes less divergent for thinner targets. For $d_0 \leqq 20$ nm, a halo surrounds the central beam with a filamented structure. The filamentation is not transposed onto the central beam. By $E = 15$ MeV, the distinct central beam has disappeared in all but the thinnest targets, leaving a more divergent lower flux beam. This is distinct from a lower flux beam with a very smooth transverse profile visible over a number of layers at the rear of the stack, which would correspond to proton energies significantly higher than observed on the TP. Hence since this feature cannot be protons, it is inferred to be due to electrons. This beam is shown in the supplemental data.

We note that the dose deposited in the RCF film in this region at $E = 9$ MeV is comparable to the dose at $E = 4$ MeV (figure 2, bottom row), even though the dose in the 4 MeV film is additionally affected by protons with energies between 4 and 9 MeV. This indicates that the proton spectrum is highly non-thermal. As the RCF stack was not sufficiently resolved to adequately sample the energy spectrum, the TP data was used to give higher resolution spectral measurements. However due to the large spatial variations in the proton beam profiles, care must be taken to correlate the TP data with specific features from the RCF images.

Proton spectra from all three TPs for $d_0 = 20$ nm (CP) are given in figure 3(a), showing a pronounced peak with energy $E_p = 8$ MeV, and energy spread $\Delta E \approx 4$ MeV, but only at 0°. Evidently this spectral peak corresponds to the central beam observed in the beam profiles in figure 2(a)–(d). The peaked spectrum is also compared with on-axis spectra for $d_0 = 5,\ 20,\ 20,\ 100$ nm (CP, CP, LP, LP) in figure 3(b). Using the beam divergence from the 9 MeV profile, and integrating the spectrum gives $(3 \pm 1) \times 10^{11}$ protons ≈50 nC within the spectral FWHM for $d_0 = 20$ nm, with a conversion efficiency of laser energy ≈0.25%. We note that spectrally peaked proton beams of similar energies were generated down to $d_0 = 5$ nm. This suggests that the laser prepulse or rising edge does not destroy the target prior to the peak of the pulse, which would result in reduced efficiency for ion acceleration for the thinnest targets [22].

The corresponding carbon spectra are also plotted. They are thermal with a maximum velocity $v_{cf} \approx 3 \times 10^7$ ms^{-1} corresponding to the start of the proton peak. The protons in the peak have outrun the C^{6+} front. This explains why the profiles for these central beams shown in figure 2 are free from instabilities experienced by the carbon plasma, since the carbon front would act as a barrier to laser driven instabilities.

On shots featuring the bright central beams, a highly divergent but comparatively low flux proton beam was also measured on the TP, reaching energies ($E_{max} \approx$ 20–30 MeV). This is visible on the $E \approx 15$ MeV profiles in figure 2, and was sufficiently divergent to be observed on the 20° TP, outside the ring.

The variation of the energy of the proton beam, E_p, and energy spread, ΔE, with d_0 is shown in figure 4(a). Both laser polarisations showed similar results for $d_0 \in$ 20–100 nm, and for this range the data points represent the mean of both LP and CP. The graph is composite from 15 shots; the standard deviation of the repeat measurements is indicated by the vertical bars. Of these, 11 shots between 10 and 100 nm showed a clear central beam on the RCF combined with spectral peaks on the TP. A lack of sensitivity to polarisation has been observed previously for ultra-thin foils, and was attributed to target deformation negating the desired electron heating suppression for CP [10, 30]. However for $d_0 = 5$ nm, only CP resulted in spectrally peaked beams; LP produced a thermal spectrum with $E_{max} \approx 5$ MeV, significantly lower than that for CP and shown as a separate data point. No peak was observed for $d_0 = 500$ nm. Also plotted in figure 4(a) are the maximum carbon and proton energy

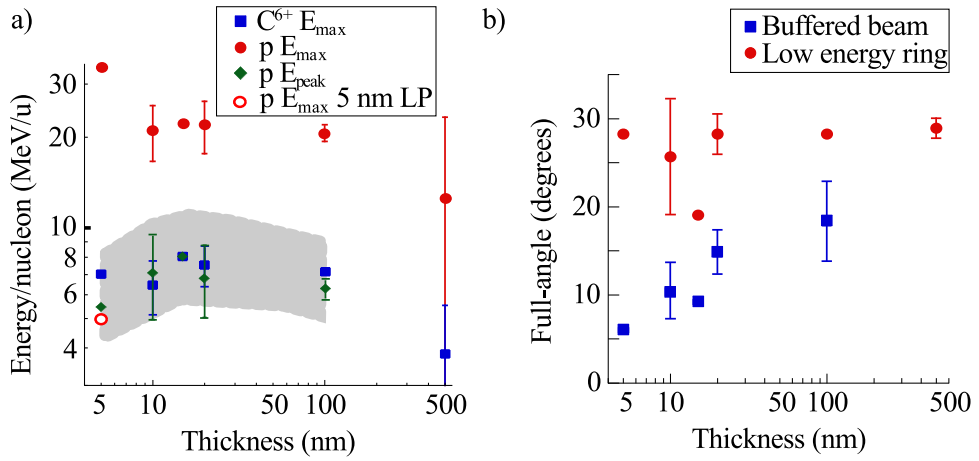

Figure 4. As a function of d_0: (a) maximum energy per nucleon for H^+ (filled red circles, with empty red circle for 5 nm LP) and C^{6+} (blue squares) and energy of H^+ peak (green diamonds) with FWHM energy spread shaded grey; (b) divergence of central beam (blue squares, at $E = 9$ MeV) and low energy ring (red circles, at $E = 4$ MeV). Vertical bars are the *standard deviation* of multiple shots.

per nucleon, E_{max}, as observed on any TP, averaged over multiple shots. The maximum energy was most often off-axis on the 20° TP, as has previously been reported from relativistically transparent targets [23]. E_{max} for the C^{6+} ions correlates well with E_p, confirming the velocities are linked.

Figure 4(b) shows that the divergence of the central beam decreases with decreasing d_0, as apparent in figures 2(a)–(d), down to ≈8° for $d_0 = 5$ nm. By contrast, the low energy ring divergence, measured at 4 MeV, remains at $26 \pm 5°$, again indicating that these are separate populations.

3. Numerical simulation and interpretation

To understand the mechanism by which these high charge narrow energy spread proton beams were produced, representative simulations were run with the 2D particle-in-cell (PIC) code OSIRIS [31] in a box of 160×80 μm with cell size 4×10 nm. The target was composed of 90/10% of C^{6+}/H^+ by charge density with $n_e = 1000 n_c$, and 2500 particles per cell per species. Resolution and particles per cell were optimised by convergence scans, and care was taken to ensure the simulation box was large enough to not influence dynamics. The boundaries were absorbing for particles and fields. The initial density was set slightly higher than DLC ($\rho \approx 2.8$ g cc^{-1}, $n_e \approx 850 n_c$) to account for the hydrocarbon impurity layer. Initial target thickness d_0 was varied between 5 and 100 nm. The electron temperature was initialised at $T_{e0} = 200$ eV for numerical reasons, resulting in target expansion before the arrival of the laser of approximately 50 nm $\approx 2 c_s \tau_a$, where τ_a is the simulation time before the pulse reaches the target. Although the effective initial target thickness is therefore larger than initialised, the areal density remains consistent with the experimental parameters. The initial target temperature relaxes the resolution constraints, and the effect of changing the initial temperature has been previously investigated [22]. The laser was initialised from an antenna located on the boundary with CP or LP and gaussian transverse and longitudinal field profiles with $w_0 = 22$ μm, $\tau_L = 650$ fs, and $a_0 \equiv eE_0/mc\omega_0 = 3$: $I_L \approx 10^{19}$ W cm^{-2}. Although this exceeds the experimental focal spot size at low power, we note that the high power focal spot was not measured experimentally, and could vary significantly due to the differences in the laser phase front combined with the expansion of the plasma mirror over the ≈1 ps pulse. We also note that 2D simulations are likely to underestimate target decompression therefore overestimating accelerating fields in the expanding sheath, and may also affect plasma heating dynamics particularly for CP. However, 3D simulations of the interaction at sufficient resolution are prohibited by computational constraints. As will be shown, the focusing parameters provide the best match to the experimental results, and therefore likely give the best description of the plasma dynamics relevant to our experiment.

For $d_0 = 10$ nm, early-on all the electrons in the focal spot are heated to the instantaneous ponderomotive potential and sheath formation is enhanced. The target expands during the rising edge of the laser from sheaths at both surfaces. As a result the longitudinal field within the target passes through zero, and in this phase most protons remain within the target. This is different to the case where the target remains comparable in size to the initial skin depth as in RPA schemes, where species separation is almost instantaneous [8, 9].

As the laser intensity increases, the radiation pressure, P_R, of the pulse exceeds the plasma thermal pressure P_t, or $I_L(t)/c > n_e(t) k_b T_e(t)$, and the front surface recedes. In this stage, the front surface is prone to transverse instability [18], enhancing target decompression and quickly causing it to become transparent. The electron and

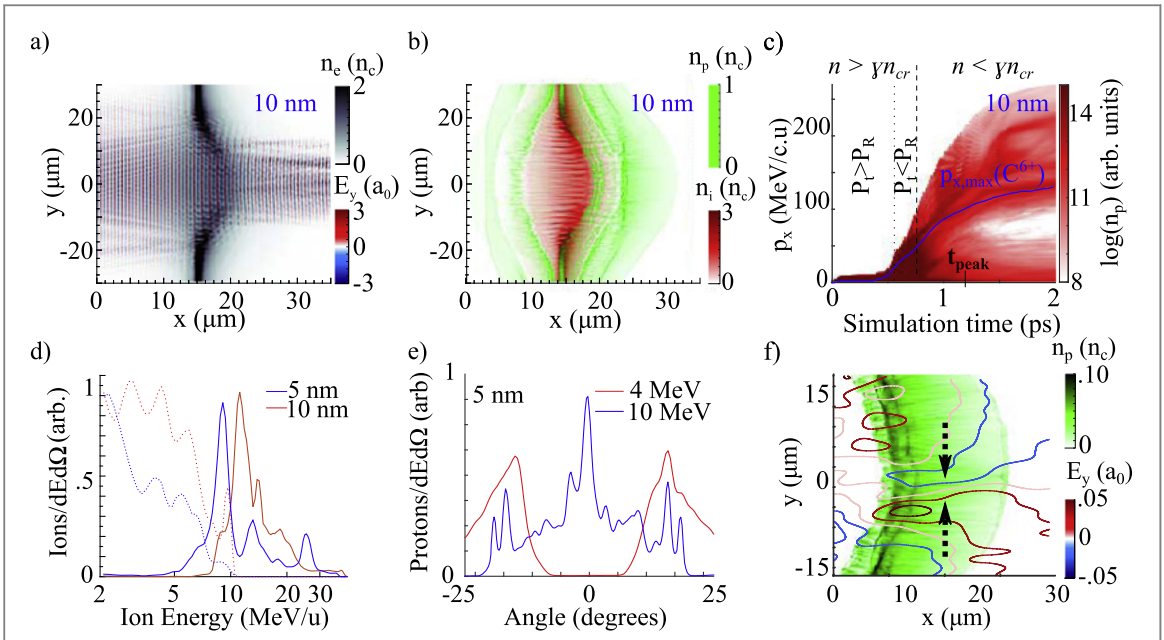

Figure 5. From simulation: (a) charge density of electrons and overlaid transverse electric field E_y showing target transparency, and (b) charge density of C^{6+} (red) and protons (green) near the peak of pulse, t_{peak}, for $d_0 = 10$ nm; (c) evolution of p_x for protons on-axis, with $p_{x,max}$ for C overlaid (blue line) for $d_0 = 10$ nm; vertical dashed (dotted) lines indicate different density (pressure) regimes; (d) spectra of protons (solid) and C^{6+} (dotted) witnessed in ≈1 msr on-axis for $d_0 = 5,\ 10$ nm; (e) angular proton distribution at 4 and 10 MeV for a 5 nm target; (f) n_p at $t_{peak} + 200$ fs with overlaid electrostatic E_y contours for $d_0 = 5$ nm.

ion density in this phase is shown in figures 5(a) and (b), together with the transverse electric field E_y showing laser transmission through the target. Ponderomotive pressure inhibits the front surface sheath, and an almost uniform capacitor-like E_x field is produced through-out the transparent region due to hot-electrons exiting the rear-surface.

Due to their higher charge-to-mass ratio, protons inside the carbon plasma respond more quickly to this bulk field and outrun the C^{6+} ions (figure 5(c)), gaining a minimum velocity equal to that at the C^{6+} ion front, v_{cf}. This results in an abundance of protons with $v_p \gtrsim v_{cf}$. Since $v_p/v_c = 2$ due to different charge-to-mass ratios, total species separation occurs if $d/2 \lesssim \int_0^\tau (v_p - v_c)\mathrm{d}t = \int_0^\tau v_p(t)\Big/2\mathrm{d}t$, where d is the target thickness when the bulk field is generated and τ is the acceleration time. From the simulations, the time-average field during acceleration is $E_{xb} \approx 6 \times 10^{11}$ V m^{-1}, and lasts for $\tau \approx 750$ fs. Assuming a static potential, the minimum target thickness for proton expulsion is therefore $d \lesssim (e/m_p)E_{xb}\tau^2/2 \approx 15\ \mu$m, much greater than $d \approx d_0 n_0/\gamma n_c \approx 3\ \mu$m at the time the target becomes transparent in the simulation for this initial $d_0 = 20$ nm foil.

Modulated spectra have been reported previously due to acceleration of comoving protons close to a high-Z ion front [32–35], where only a small fraction of the protons are affected. These simulations however show a *bulk* field which causes almost complete expulsion of protons from the target. Indeed, we note that for such thin targets, the initial spatial location of the hydrogen, either in the bulk or on the target surface, makes little difference to the late-time dynamics. Figure 5(c) shows the temporal evolution of the on-axis forward momentum p_x of the protons with $p_{x,max}$ of the C^{6+}. The ion energy gain occurs mostly when the target is transparent, and is not due to RPA [22], unlike previous reports of species separation from ultra-thin targets [10, 11]. Below v_{cf} there are almost no protons, resulting in peaked on-axis spectra (figure 5(d)), as measured experimentally.

This species separation occurs for all target thicknesses up to 100 nm. For $d_0 = 100$ nm, the target remains overdense and protons are not completely driven out, unlike for $d_0 < 20$ nm. However, there is still significant species separation at the sheath front due to the large Debye length, manifesting in a spectral peak in the proton beam matched to the maximum carbon energy. Further simulations with the addition of a hydrogen-rich surface contaminant layer to the target enhances the proton number in this peak, but such contaminant layers are not necessary to observe this effect. Species separation is most prominent for the thinnest targets, which may indicate why spectrally modulated beams were not observed at $d_0 = 500$ nm.

At later times, the minimum proton energy in the buffered layer increases, giving a proton peak energy E_{peak} that follows the carbon front velocity v_{cf}. Simultaneously the maximum energy of the tail of the proton distribution E_{max} increases due to acceleration in the sheath, leading to a high energy proton tail beyond the peak

with wide divergence, as witnessed experimentally. Though the carbon plasma exhibits transverse spatial modulation, most of the protons have been shielded from this filamentation, as can be seen by comparison of the spatial properties of the two species in figure 5(b).

Expulsion of protons from the carbon plasma results in strong angular beam dependence on proton energy, as seen for $d_0 = 5$ nm at the end of acceleration (figure 5(e)). At low beam energies, equivalent to the 4 MeV layer in the RCF, no axial protons are observed. In the initial expansion phase, electron heating is localised to a small transverse extent similar to the longitudinal size of the expanding plasma $\sim w_0$. The transverse to longitudinal electric field ratio $E_y/E_x \approx \frac{\partial n_e}{\partial y}\Big/\frac{\partial n_e}{\partial x} \sim \frac{1}{3}$ results in rapid transverse expansion [36]. The remnants of this initial expansion are responsible for the ring observed experimentally at low energy, and the cone-like expansion visible on the optical probe. The low axial density of the expansion measured from the interferometry is therefore likely to be caused by this transverse expansion, and can be enhanced by laser propagation through the relativistically transparent region [37].

At higher energies, a low divergence component ($\approx 5^\circ$) close to the laser-axis becomes apparent, consistent with the central beams seen experimentally. The sheath of the self-generated cone has a focussing effect on protons still being accelerated within the evacuated region, similar in action to other laser-triggered charged particle lenses [38, 39]. The focussing field, shown in figure 5(f), is maintained until the end of the interaction, producing a collimated beam on-axis. For thicker targets, there are sufficient protons in the target that a larger fraction remain in the central region, reducing the collimating effect. A static B-field of magnitude $\approx$2 kT also forms, and though providing an order of magnitude lower force on the protons than the electric field, acts to pinch the forward laser driven relativistic electrons, further enhancing the space charge collimating fields during the laser plasma interaction. Note that only the protons nearest the laser-axis are refocused by this collimating field; further off-axis more divergent protons continue to be accelerated in the hot electron driven sheath fields to high energies. As previously discussed, such a highly divergent but lower flux beam was also witnessed in the experiment.

LP simulations showed only minor differences from CP; the target became transparent slightly earlier ($\sim$150 fs $\ll \tau_L$). In both cases, the laser–plasma interface quickly deforms, reducing the electron heating suppression expected for CP. This explains the lack of dependence on polarisation in the experiment, except for the very thinnest targets where LP causes the target to become too underdense by the peak of the pulse, resulting in negligible acceleration [22].

Further simulations were performed for $d_0 = 20$ nm, varying laser intensity and w_0 while keeping the 2D transverse integral constant, equivalent of fixing the laser power and varying focusing. For $a_0 < 2$, the target remains overdense, radiation pressure never overcomes plasma pressure, and buffering is not observed. For $a_0 > 3$, the target becomes transparent before the peak of the pulse, and both species gain energy during relativistic transparency, as in figure 5(c). However, for $a_0 = 8.5$ as should be implied from our experimental low power focal spot measurement ($w_0 = 8\ \mu$m), $E_p = 35$ MeV. The lower experimental value therefore implies a lower focal intensity, likely due to poor laser near-field uniformity combined with hydrodynamic expansion of the plasma mirror for $\tau_L \approx 1$ ps.

For fixed target thickness d_0 and varying the normalised vector potential from $a_0 = 2$ to $a_0 = 10$, the simulations suggest a scaling $E_p \propto a_0$, following the ponderomotive scaling typical of thermally driven acceleration. Varying w_0 with fixed a_0 makes no appreciable difference to E_p. However, E_p is dependent on the ratio of carbon to proton mass in the target [24], with a trade-off between higher energy but fewer protons. Further simulations performed with near optimal parameters for the Vulcan Petawatt system ($a_0 = 11$, $w_0 \approx 8\ \mu$m, $d_0 = 20$ nm) resulted in $E_p \approx 50$ MeV, and $E_{max} > 100$ MeV.

4. Conclusions

We have demonstrated the generation of high charge, narrow energy-spread proton beams for the first time from an initially homogenous thermally expanding plasma. The beams are produced by the irradiation of ultra-thin foils (5–100 nm) with an intense ($>10^{19}$ W cm^{-2}) laser. Due to their higher charge-to-mass ratio, these proton beams are buffered ahead of, and protected from, transverse Rayleigh–Taylor-like instabilities in a more slowly expanding carbon plasma. For reducing target thickness, the buffered beam reduces in divergence down to $\approx$8° for a 5 nm target. 2D particle-in-cell simulations reveal the increased beam collimation is due to a plasma space-charge lensing effect, and also demonstrate this mechanism can be scaled to higher laser intensity with proton energies $\propto a_0$. The contrasting spectral characteristics of the ring and central beam highlight the importance of combined beam profile and spectral measurements when reporting narrow energy spread ion beams, as the properties of the whole beam cannot be extrapolated by integrating over the whole beam, or indeed by sampling over limited angular acceptance. Importantly, this method of generating narrow energy spread beams produces high charge ($\approx$50 nC) beams without the added complexity of microstructured targets in

previous experiments on spectrally peaked beams from thermal acceleration [3–5]. Our demonstration of buffered acceleration from relativistically transparent targets will therefore be attractive for nuclear physics applications.

Acknowledgments

We acknowledge funding by EPSRC/RCUK grants EP/E035728/1, EP/K022415/1 and STFC grant ST/J002062/1. We thank the Osiris consortium (UCLA/IST) for use of Osiris, and the support of the LMU's MAP-service centre to provide DLC foils.

References

[1] Clark E L *et al* 2000 *Phys. Rev. Lett.* **84** 670
[2] Snavely R A *et al* 2000 *Phys. Rev. Lett.* **85** 2945
[3] Schwoerer H *et al* 2006 *Nature* **439** 7075
[4] Hegelich B *et al* 2006 *Nature* **439** 7075
[5] Pfotenhauer S M *et al* 2008 *New J. Phys.* **10** 3
[6] Dollar F *et al* 2011 *Phys. Rev. Lett.* **107** 065003
[7] Yin L *et al* 2007 *Phys. Plasmas* **14** 056706
[8] Qiao B *et al* 2010 *Phys. Rev. Lett.* **105** 155002
[9] Yu T P, Pukhov A, Shvets G and Chen M 2010 *Phys. Rev. Lett.* **105** 065002
[10] Kar S *et al* 2012 *Phys. Rev. Lett.* **109** 185006
[11] Steinke S *et al* 2013 *Phys. Rev. STAB* **16** 011303
[12] Zhang X *et al* 2007 *Phys. Plasmas* **14** 123108
[13] Esirkepov T *et al* 2004 *Phys. Rev. Lett.* **93** 175003
[14] Robinson A P L *et al* 2008 *New J. Phys.* **10** 013021
[15] Yan X Q *et al* 2008 *Phys. Rev. Lett.* **100** 135003
[16] Klimo O *et al* 2008 *Phys. Rev. STAB* **11** 031301
[17] Henig A *et al* 2009 *Phys. Rev. Lett.* **103** 245003
[18] Palmer C A J *et al* 2012 *Phys. Rev. Lett.* **108** 225002
[19] Willingale L *et al* 2009 *Phys. Rev. Lett.* **102** 125002
[20] Henig A *et al* 2009 *Phys. Rev. Lett.* **103** 045002
[21] Yin L *et al* 2006 *Laser Part. Beams* **24** 291
[22] Yin L *et al* 2011 *Phys. Plasmas* **18** 063103
[23] Jung D *et al* 2013 *New J. Phys.* **15** 023007
[24] Jung D *et al* 2013 *Phys. Plasmas* **20** 083103
[25] Thaury C *et al* 2007 *Nat. Phys.* **3** 424
[26] Ma W *et al* 2011 *Nucl. Instrum. Methods Phys. Res.* A **655** 53
[27] Nürnberg F *et al* 2009 *Rev. Sci. Instrum.* **80** 3
[28] Kar S *et al* 2008 *Phys. Rev. Lett.* **100** 225004
[29] Mančić A *et al* 2008 *Rev. Sci. Instrum.* **79** 073301
Doria D *et al* 2009/10 *CLF Annual Report* RAL, UK p 78
[30] Dollar F *et al* 2012 *Phys. Rev. Lett.* **108** 175005
[31] Fonseca R A *et al* 2002 *Lecture Notes in Computer Science* vol 2331 (Berlin: Springer) p 342
[32] Decoste R and Ripin B H 1978 *Phys. Rev. Lett.* **40** 34
[33] Allen M *et al* 2003 *Phys. Plasmas* **10** 3283
[34] Bychenkov V Yu *et al* 2004 *Phys. Plasmas* **11** 3242
[35] Robinson A P L, Bell A R and Kingham R J 2006 *Phys. Rev. Lett.* **96** 035005
[36] Bin J H *et al* 2013 *Phys. Plasmas* **20** 073113
[37] Powell H W *et al* 2015 *New J. Phys.* **17** 103033
[38] Toncian T *et al* 2006 *Science* **312** 410
[39] Kar S *et al* 2008 *Phys. Rev. Lett.* **100** 105004